Materials and Design 191 (2020) 108622

Contents lists available at ScienceDirect

Materials and Design

journal homepage: www.elsevier.com/locate/matdes

# Deformation mechanisms in a superelastic NiTi alloy: An in-situ high resolution digital image correlation study

E. Polatidis [a], M. Šmíd [a], I. Kuběna [a,b], W.-N. Hsu [a,c], G. Laplanche [d], H. Van Swygenhoven [a,c,*]

[a] Photons for Engineering and Manufacturing, Swiss Light Source, Paul Scherrer Institute, CH-5232 Villigen PSI, Switzerland
[b] CEITEC IPM, Institute of Physics of Materials AS CR, v.v.i., Žižkova 22, 616 62 Brno, Czech Republic
[c] Neutrons and X-rays for Mechanics of Materials, IMX, École Polytechnique Féderale de Lausanne, CH-1015 Lausanne, Switzerland
[d] Institut für Werkstoffe, Ruhr-Universität Bochum, Universitätsstr. 150, 44780 Bochum, Germany

## HIGHLIGHTS

- High-resolution digital image correlation is used to unveil the deformation mechanisms that occur in superelastic NiTi.
- Deformation mechanisms: those resulting in non-recoverable strain and martensite formation resulting in recoverable strain.
- Good agreement with Schmid law for the martensite transformation and with the theoretical transformation strain is seen.

## GRAPHICAL ABSTRACT

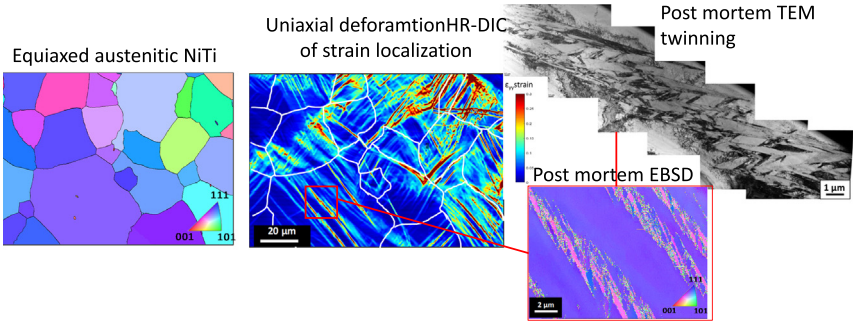


## ARTICLE INFO

*Article history:*
Received 3 October 2019
Received in revised form 27 February 2020
Accepted 2 March 2020
Available online 5 March 2020

*Keywords:*
DIC
EBSD
Phase transformation
NiTi
Schmid factor

## ABSTRACT

An in-situ high resolution digital image correlation investigation during uniaxial tensile deformation reveals the recoverable and the non-recoverable strain mechanisms in a $Ni_{51}Ti_{49}$ alloy with a mean grain size of 35 µm. Recoverable strain is due to the martensitic transformation, for which more than one variant per grain can be activated. The majority of the activated variants exhibit high Schmid factor. The variant selection can be influenced by shear transmission across grain boundaries, when the geometrical compatibility between the neighboring habit plane variants is favourable; in these cases variants that do not have the highest Schmid factor, with respect to the macroscopically applied load, are activated. The experimentally determined transformation strains agree well with theoretical calculations for single crystals. The non-recoverable strain is due to deformation slip in austenite, twinning in martensite and residual martensite. The results are discussed in view of possible twinning modes that can occur in austenite resulting in significant non-recoverable strain.


## 1. Introduction

NiTi alloys in near-equiatomic compositions are well known for their superelasticity which results from the reversible austenite-martensite transformation. These alloys can be found in various applications including biomedical [1], actuators and robotics [2]. The deformation behaviour of NiTi strongly depends on the crystallographic orientation

* Corresponding author at: Photons for Engineering and Manufacturing, Swiss Light Source, Paul Scherrer Institute, CH-5232 Villigen PSI, Switzerland.
*E-mail address:* helena.vanswygenhoven@psi.ch (H. Van Swygenhoven).

https://doi.org/10.1016/j.matdes.2020.108622

with respect to the loading direction in single crystals [3,4], and the crystallographic texture in polycrystalline alloys [5]. The martensitic variants have been determined by the characterization of the shear bands and their inclination with respect to the loading direction in combination with the Schmid factor. Such experiments have been carried out under tension, compression [6,7] and nanoindentation [8] using SEM/EBSD. During loading, martensite variants with the highest Schmid factor are first activated [5], but usually more than one martensite variant may form in each austenite grain [7]. During reverse transformation, both favourable and less-favourable variants contribute to the recovered strain [5].

TEM results have shown that dislocations slip, twinning and residual martensite are responsible for non-recoverable strains and loss of superelasticity [9–16], though, how these deformation mechanisms cooperate at the mesoscopic level, where grain-to-grain interactions can affect the activation of these mechanisms, is not clear. HR-DIC in SEM has recently become a powerful tool with sub-micron spatial resolution to study the activation of slip in various steels [17–22], Ti-alloy [23], Mg alloys [24] and the fracture mechanics in oxide layers [25]. Conventional DIC [26–28] and HR-DIC [29,30] have also been applied to investigate the martensitic transformation in NiTi. However, the low density of the DIC speckle pattern did not allow achieving the necessary resolution for characterizing the martensite variants and the reversible transformation strain of individual variants. Recently HR-DIC and EBSD have been combined to study the martensitic transformation during multiaxial loading and strain path changes in a superelastic NiTi alloy having a microstructure composed of nanocrystalline substructures [31]. By correlating HR-DIC strain maps to the EBSD data, it was found that bands of nanocrystalline austenite grains transform collectively into martensite.

HR-DIC can quantify the strain magnitude of the austenite to martensite transformation and the recoverable strain upon unloading. Comparing recoverable and non-recoverable strain allows the identification of the coexisting deformation mechanisms in addition to the martensitic transformation, such as slip [12] or deformation twinning [13–16,32,33]. This information is essential for developing and informing existing phase-field models that incorporate mechanisms of multi-variant phase transformations and polytwinning [34–37].

The objective of this study is to perform HR-DIC on a coarse-grained superelastic NiTi alloy to reveal the deformation mechanisms resulting in recoverable and non-recoverable strain. Using a dense silica speckle pattern, HR-DIC allows the characterization of the activated habit plane variants, the slip planes and the deformation twinning. Moreover, it allows the direct measurement of the transformation strain originating from the activated variants. Such information is essential for improving the analytical tools for predicting the mechanical behaviour of NiTi that up to now rely on simplified assumptions for the micromechanical response of the material.

## 2. Materials and methods

### 2.1. Experimental procedures

A rectangular ingot ($20 \times 76 \times 90$ mm$^3$) with nominal composition $Ni_{51}Ti_{49}$ (in at.%) was produced by vacuum induction melting using nickel (Ni purity >99.98 wt%) and titanium (Ti purity >99.995 wt%) at the Ruhr-University Bochum (Germany). Melting was performed in a graphite crucible using a VSG 010 furnace from PVA TePla AG in a high-purity Ar Atmosphere (99.998 vol%) under a pressure of 500 mbar. The melt was then poured into a pre-heated mould (500 °C) that had been coated with an yttria slurry. The ingot was solution heat treated for 5 h at 1000 °C under an argon atmosphere with a constant flow rate of 4 dm$^3$/min. The thickness of the cast ingot was then reduced in 22 steps from 20 mm to 1.8 mm by hot rolling at 800 °C (thickness reduction: 90%). Prior to each step, the $Ni_{51}Ti_{49}$ sheet was annealed for 10 min at 800 °C. The 1.8 mm sheet was further rolled at room temperature in three steps into a thinner sheet (thickness: 1.2 mm, thickness reduction: 30%). Between each cold rolling step, the $Ni_{51}Ti_{49}$ sheet was annealed for 10 min at 800 °C followed by water quenching. After cold rolling, the 1.2 mm $Ni_{51}Ti_{49}$ sheet was recrystallized for 10 min at 800 °C and water quenched. More details about the microstructure and texture of the recrystallized $Ni_{51}Ti_{49}$ sheet can be found in Ref. [38]. The stress strain curve of a 1 mm thick sample deformed under uniaxial tensile loading is given in Fig. S1 of the Supplementary material. The maximum superelastic strain amounts 5.5% as evident by the dip in the stress/strain curve indicating the end of the stress plateau and the onset of the deformation of the stress-induced martensite.

The geometry of the dog-bone shaped tensile specimen used in the HR-DIC experiment is given in Fig. S2 of the Supplementary material. The specimens were cut parallel to the rolling direction of the sheet, using a picosecond laser at the Swiss Federal Laboratories for Materials Science and Technology (EMPA). The surfaces of the tensile specimens were mechanically ground (with 600, 1200, 2500, 4000 grid SiC papers) and one of the surface was further polished with diamond-suspension (3 μm and 1 μm) followed by final polishing using a vibratory polisher (Buehler Vibro-Met2 using a suspension Buehler Mastermet2 with a particle size of 0.02 μm for 24 h). The final thickness of the tensile specimen is approximately 80 μm. Based on the average grain size and the sheet thickness, two to four grains are contained within the thickness of the tensile specimen.

EBSD investigations on the region of interest for HRDIC were performed at the centre of the dogbone sample using a field emission gun scanning electron microscope (FEG SEM) Zeiss ULTRA 55 equipped with EDAX Hikari Camera. The microscope was operated at 20 kV in high current mode with 120 μm aperture. The electron backscatter patterns were acquired by the TEAM software with $4 \times 4$ pixels binning and the crystal orientation was determined by 8 indexed Kikuchi bands for each pattern. The step size of the mapping varied from 150 to 60 nm, according to the size of the region of interest. The EBSD raw data were post-processed using the EDAX OIM Analysis 7.3 software.

Producing dense speckle patterns for HRDIC is challenging and many methods have been proposed in the literature [17,39–41]. In the present work, patterns for HR-DIC were applied by rotating the samples on a polishing cloth with a few droplets of OPS suspension (from Microdiamant GmbH with a particle size of 0.04 μm) and subsequently cleaned with deionized water, as described in [22]. The advantage of this method is that it allows performing EBSD while the speckle pattern still remains on the sample surface. This process results in sub-micron resolution of the DIC method. The tensile sample was deformed up to a maximum force of 32 N using the mini-biaxial machine described in [42] mounted on the Zeiss ULTRA 55 stage. During the tensile deformation, a macroscopic Lüders band formed as typically seen in superelastic [26–28,43–45] and shape memory NiTi alloys [46,47]. The front of the Lüders band propagated along the HR-DIC field of view (FOV) with an inclination of ~46° with respect to the loading direction (as shown in the schematic of Fig. 1c), as typically seen in sheet samples [48]. In NiTi wires, the front of the Lüders band is perpendicular to the loading direction [49].

HR-DIC measurements were performed at the centre of the gauge length at two loading states: (1) when the Lüders band reached the area of interest corresponding with 8% average strain in the FOV (as shown in the schematic of Fig. 1c) and (2) when the Lüders band had passed through the area of interest, with average strain of 10% within the FOV. The strain within the Lüders band is typically similar to the strain reached at the end of the plateau [28,47]. In the present work however, the average strain within the FOV reached 10%, while the plateau strain is 5.5% (as shown in Fig. S1 of the Supplementary material). This discrepancy can be explained in two ways. First by considering the limited number of grains (2–4) through the sample thickness as a result of the relatively large grain size and the thin sample thickness. Sutou et al. [50] showed that the relative grain size with respect to the sample thickness can greatly affect stress/strain characteristics. Secondly, the

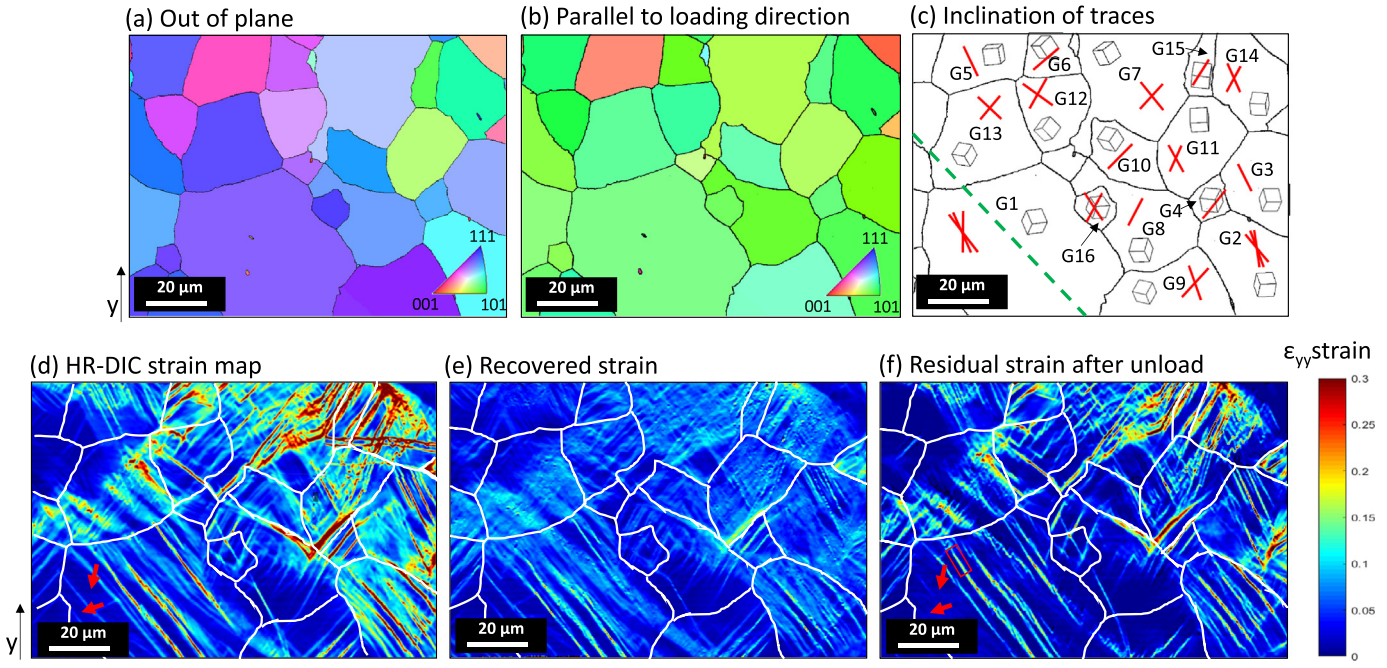


**Fig. 1.** EBSD maps of the region of interest (a) out of plane projection and (b) loading direction projection respectively shown with inverse pole figure colour coding. (c) Microstructure illustrating the unit cell orientation and the inclination of the traces seen in (d) in each grain. The grains are labelled from 1 to 16 and the y-axis corresponds to the loading direction. The green dashed line shows the position of the Lüders band front at 8% average strain within the FOV (d) HR-DIC map at maximum load (i.e. average strain of 10%). (e) Map of recovered strain calculated by mathematical subtraction of the map shown in (d) minus the map shown in (f). (f) Map of residual strains after complete unloading. The red square indicates the location that a TEM lamella was extracted from. The red arrows indicate traces (in d) that completely vanished after unloading (in f) due to the reversible phase transformation.

sample might contain thickness variations, which cause local stress concentrations and locally high strains possibly beyond the superelastic limit of the material. As the material is seen to exhibit significant non-recoverable strain, the latter probably occurs, and it is further discussed in Section 4.2. The images for the HR-DIC analysis were acquired with a Zeiss ULTRA 55 FEG-SEM using an in-lens secondary electron detector at 6.9 mm working distance with 3 kV acceleration voltage and an aperture size of 30 μm. A series of SEM images with a resolution of 3072 × 2304 pixels were taken at ×2000 magnification and with 25 μsec dwell time. The Ncorr MATLAB code [51] was used for the HR-DIC analysis using a subset size of 15 pixels and subset spacing of 1 pixel. Previous HR-DIC measurements [21] have shown that the error due to drift and lens distortion is insignificant, compared to the magnitude of strains of slip and transformation bands, and therefore no corrections have been applied. The identification of the grain boundaries on the HRDIC map is challenging due to the high deformation and rotation of the grains. This is done using the position of the grain boundaries in the undeformed sample obtained from EBSD and the usage of the open source python code, DefDap [52].

The surface of the unloaded dogbone was re-polished using diamond paste (with particle size of 1 μm and 0.25 μm) followed by a final vibration polishing for 24 h in order to smoothen the deformation-induced surface relief and to achieve better surface quality for post-mortem EBSD investigations. Although some material was removed from the surface, the same grains as seen with HR-DIC could be observed the post-mortem in EBSD investigation.

Transmission electron microscopy (TEM) characterization was undertaken using a JEOL-2010 microscope operated at 200 kV. TEM sample was prepared by extracting a rectangular lamella from the surface plane in grain 1 as shown in Fig. 1f, and milling it using a focused ion beam (FIB) on a Zeiss NVision-SEM/FIB. The FIB-milling was undertaken using a 30 kV and 3 nA FIB. After the lift-out, the lamella was thinned by FIB using 30 kV and successively 700 pA, 300pA and 80 pA current as the thickness was reducing. The final surface cleaning was done using a 5 kV and 100 pA FIB.

### 2.2. Habit plane traces analysis

Upon loading, the austenite (cubic B2 phase, ordered BCC) transforms into twinned martensite (monoclinic B19' phase) bands where the interface between the austenite and the twinned martensite is an invariant plane also called the habit plane. In the present work, we consider only type II twinning, since the latter has been found to be a dominant twinning mode in SE NiTi alloys under deformation [11]. This type of twinning has also been seen to agree well with the habit-plane variants (HPVs) in polycrystalline materials under deformation [4,6–8]. The HPVs, also called correspondent-variant pair (CVP), of type II twinning {0.8684 0.2688 0.4138}⟨−0.4580 0.7706 0.4432⟩ are listed in Table 1 using the experimentally determined systems in [53]. Note the that indices of the habit plane and those of the twinning shear direction were normalized and that they are all expressed in the coordinate system of the B2 austenite. It is also noted that although the HPVs in Table 1 were identified in single crystals for thermally-induced martensite [54], they agree well with the observed stress-induced HPVs in [6–8].

The inclination of the habit plane trace with respect to the loading direction can be calculated as follows [7]: The habit plane $m$ and the transformation shear direction $b$ of the shape strain is given in the form: $(h\ k\ l)_\alpha[u\ v\ w]_\alpha$ (where $\alpha = 0, 1, 2,\ldots 24$), for the 24 possible habit plane variants. The orientation of the parent B2 phase is given in the form: $[HKL]_\beta$ $[U\ V\ W]_\beta$ for the $\beta$-th grain of a polycrystal, where $[H\ K\ L]$ and $[U\ V\ W]$ are the normal direction of the grain and the tensile direction of the grain, respectively. A list of the normal and the loading directions for all the investigated grains is given in Table S1 of the Supplementary material. The habit plane trace direction of the $\alpha$-th variant in the $\beta$-th grain is then given by the cross product [7,55]:

$$\left[R_\beta^\alpha S_\beta^\alpha T_b^\alpha\right] = [hkl]_\alpha \times [HKL]_\beta \quad (1)$$

**Table 1**
The 24 habit plane variants (also called correspondent variant pairs) using the notation from [54] and the experimentally determined system for the habit plane/invariant shear direction from [53].

| Variant, notation from [54] | Habit plane | Invariant shear direction |
|---|---|---|
| 1(+) | (0.8684 0.2688 −0.4138) | [−0.458 0.7706 −0.4432] |
| 1(−) | (0.8684 0.4138 −0.2688) | [−0.458 0.4432 −0.7706] |
| 1′(+) | (−0.8684 0.4138 −0.2688) | [0.458 0.4432 −0.7706] |
| 1′(−) | (−0.8684 0.2688 −0.4138) | [0.458 0.7706 −0.4432] |
| 2(+) | (0.8684 0.2688 0.4138) | [−0.458 0.7706 0.4432] |
| 2(−) | (0.8684 0.4138 0.2688) | [−0.458 0.4432 0.7706] |
| 2′(+) | (−0.8684 0.4138 0.2688) | [0.458 0.4432 0.7706] |
| 2′(−) | (−0.8684 0.2688 0.4138) | [0.458 0.776 0.4432] |
| 3(+) | (−0.4138 0.8684 0.2688) | [−0.4432 −0.458 0.77706] |
| 3(−) | (0.2688 −0.8684 −0.4138) | [0.7706 0.458 −0.4432] |
| 3′(+) | (0.2688 0.8684 −0.4138) | [0.7706 −0.458 −0.4432] |
| 3′(−) | (0.4138 0.8684 −0.2688) | [0.4432 −0.458 −0.7706] |
| 4(+) | (0.4138 0.8684 0.2688) | [0.4432 −0.458 0.7706] |
| 4(−) | (0.2688 0.8684 0.4138) | [0.7706 −0.458 0.4432] |
| 4′(+) | (0.2688 −0.8684 0.4138) | [0.7706 0.458 0.4432] |
| 4′(−) | (0.4138 −0.8684 0.2688) | [0.4432 0.458 0.7706] |
| 5(+) | (0.2688 −0.4138 0.8684) | [0.7706 −0.4432 −0.458] |
| 5(−) | (0.4138 −0.2688 0.8684) | [0.4432 −0.7706 −0.458] |
| 5′(+) | (0.4138 −0.2688 −0.8684) | [0.4432 −0.7706 0.458] |
| 5′(−) | (−0.2688 0.4138 0.8684) | [−0.7706 0.4432 −0.458] |
| 6(+) | (0.2688 0.4138 0.8684) | [0.7706 0.4432 −0.458] |
| 6(−) | (0.4138 0.2688 0.8684) | [0.4432 0.7706 −0.458] |
| 6′(+) | (0.4138 0.2688 −0.8684) | [0.4432 0.7706 0.458] |
| 6′(−) | (0.2688 0.4138 −0.8684) | [0.7706 0.4432 0.458] |

where $R$, $S$, $T$ are the indices of the habit plane trace direction. The angle $\varphi_\beta^\alpha$ between the habit plane trace of the $\alpha$-th variant and the loading direction in the $\beta$-th grain is given by [7]:

$$\varphi_\beta^\alpha = \cos^{-1}\frac{R_\beta^\alpha U_\beta + S_\beta^\alpha V_\beta + T_\beta^a W_\beta}{\sqrt{\left(\left[R_\beta^\alpha\right]^2 + \left[S_\beta^\alpha\right]^2 + \left[T_\beta^\alpha\right]^2\right)\left(U_\beta{}^2 + V_\beta{}^2 + W_\beta{}^2\right)}} \quad (2)$$

The same approach can be used to calculate the trace inclination of a slip system where instead of the habit plane the slip plane is used in Eq. (1).

### 2.3. Maximum transformation strain analysis

Theoretical calculations of the transformation strains associated with Type II twinning have been shown to agree with experimentally observed transformation strains in single crystals [4,56]. Based on the formulation given in [4], by knowing the habit plane normal $m$ (with miller indices $(h\,k\,l)_\alpha$) and the transformation shear direction $b$, *(including the magnitude of shear of 0.13)*, $[u\,v\,w]_\alpha$ of the activated $\alpha$ variant, it is possible to calculate the strain matrix associated to the habit plane variant as:

$$E^\alpha = \frac{1}{2}(b\otimes m + m\otimes b + (b\cdot b)m\otimes m) \quad (3)$$

Under a certain uniaxial loading, the deformation along the loading direction is then given by:

$$\varepsilon_\beta^\alpha = e_\beta \cdot E^\alpha \cdot e_\beta \quad (4)$$

where $e_\beta$ is the crystallographic direction of the loading axis in the $\beta$-th grain [57]. Eq. (4) has been applied to each grain, $\beta$, to calculate the transformation strain that can be recovered for each habit plane variant $\alpha$. It is also worth noting that, as a first order approximation, neglecting the volume change associated with the austenite to martensite transformation, the transformation strain is directly proportional to the SF [58], i.e., $\varepsilon = SF \cdot |b|$ where $|b|$ is the magnitude of the transformation shear which is equal to 0.13 for type II twinning.

## 3. EBSD and HR-DIC results

The initial microstructure with equiaxed grains with an average grain size of ~35 μm is shown in Fig. 1a–d. The grain orientation maps (Fig. 1a and b) reveal a relatively strong ⟨111⟩-out of plane texture, as also reported in [38]. Additionally, there is a relatively strong alignment of the ⟨101⟩ direction parallel to the loading direction, see Fig. 1b. Fig. 1d shows the HR-DIC map of the deformed material at 10% strain averaged over the field of view. The grain boundaries are delineated with white lines for clarity.

As shown in Fig. 1d, the strain is accommodated heterogeneously in traces of high strain. The localized strain traces resemble the deformation bands indexed as martensite by EBSD [6,7]. The regions with low homogeneous strain are possibly retained austenite as also observed by EBSD in [6,7]. Some grains (e.g. G3, G11 and G14) exhibit high and more homogeneous strain where possibly the transformation is relatively homogenous and covers the larger area of the grains. Fig. 1e shows that significant strain is recovered upon unloading implying that the martensitic transformation is reversible, however, residual strain is also significant as seen in Fig. 1f implying that non-recoverable deformation mechanisms are operational. The observed strain traces in each labelled grain is illustrated in Fig. 1c with red lines. Besides strain traces in the grains, some amount of strain is accommodated close to the grain boundaries, see e.g. the boundary between grains G4, G8, G10 and G11, as shown in Fig. 1d.

## 4. Discussion of the deformation mechanisms

Recoverable strain is expected due to the reversible austenite-martensite phase transformation, which results in the superelasticity of the material. The presence of significant non-recoverable strain is rather unexpected considering the relatively good superelasticity shown in Fig. S1 of the Supplementary material. This can be possibly caused by small variations in thickness or width of the HR-DIC sample (Fig. S2) causing stress concentrations and local plastic deformation. Since the material locally exceeds its superelastic capability, besides the martensite formation, plastic deformation mechanisms occur. The recoverable strain traces (Fig. 1e) and non-recoverable strain traces (Fig. 1f) are discussed in detail in the following paragraphs. It should be noted that the microstructure consists of large equiaxed grains, of the order of tens of micrometres, which cannot exhibit the excellent superelastic cycling behaviour of optimized NiTi microstructures. An optimum superelastic microstructure consists of sub-grain structures of the order of nanometres in size [12,31,59].

### 4.1. Recoverable strain mechanism

#### 4.1.1. Reversible martensitic transformation

Table 2 lists the observed trace inclinations and the theoretical trace inclinations for the potentially activated habit plane variants (HPVs). It is seen that the variant selection is dependent on the orientation of the austenite grain. The theoretical transformation strains are also given in Table 2 and will be discussed in the following paragraphs. The experimental transformation strain is determined by subtracting the average strain within the strain traces (averaged using imageJ) in the unloaded state (shown in Fig. 1f) from the strain within the traces at maximum load (shown in Fig. 1d). As an example, grain G3 exhibits traces with an inclination of 153 ± 3° with respect to the loading direction. The HPV 4′(+) with the highest positive SF (SF ≈ 0.41) would result in a trace with an inclination of 152° with respect to the loading direction and theoretical transformation strain of 5.2%. The experimentally determined transformation strain is 5.6%. Note that the variant with the highest positive SF should form under tension, whereas the

**Table 2**
List of the grains and the observed trace inclinations and their correlation with the habit plane variants ranked by SF values. The list includes the theoretical transformation strain of the activated variants and the experimentally observed recovery strain. Note that the theoretical transformation strain (sixth column) is proportional to the Schmid factor (third column). The error represents the standard deviation of the inclination measured over several traces in each grain.

| Grain | Angle of trace with respect to loading direction from HR-DIC (degrees) | Highest SF variants, SF value | Theoretical trace angle of highest SF (degrees) | Possible activated variant rank of SF | Theoretical transformation strain [variant] | Recoverable strain from HR-DIC |
|---|---|---|---|---|---|---|
| G1 | 151 ± 2 | 4′(+), SF = 0.460 or | 145 or | 1st | 6.0% [4′(+)] or | 4.6% |
| | | 4′(−), SF = 0.448 | 141 | or 2nd | 5.8% [4′(−)] | |
| G2 | 143 ± 2 | 3(−), SF = 0.439 | 145 | 1st | 5.7% [3(−)] | 5.5% |
| | | 3(+), SF = 0.434 | 147 | | 5.7% [3(+)] | |
| G3 | 153 ± 3 | 4′(+), SF = 0.407 | 152 | 1st | 5.2% [4′(+)] | 5.6% |
| G4 | 37 ± 1 | 3′(+), SF = 0.463 | 39 | 1st | 5.9% [3′(+)] | 5.8% |
| G5 | 155 ± 2 | 3(−), SF = 0.355 | 154 | 1st | 4.5% [3(−)] | 3.7% |
| G6[a] | 50 ± 1 | 5(+), SF = 0.412 | 38 | | | 5.9% |
| | | ***5(−), SF= 0.406*** | 48 | 2nd | 5.2% [5(−)] | |
| G7 | 141 ± 3 | 5(+), SF = 0.416 | 145 | 1st | 5.3% [5(+)] | 6.2% |
| | 46 ± 3 | 5(−), SF = 0.400 | 46 | 2nd | 5.1% [5(−)] | |
| G8 | 29 ± 4 | 4′(+), SF = 0.412 | 147 | | 5.3% [4′(+)] | 2.6% |
| | | 4(−), SF = 0.412 | 28 | 1st | 5.3% [4(−)] | |
| G9[a] | 42 ± 1 | 4(−), SF = 0.486 | 40 | 1st | 6.3% [4(−)] | 3.4% |
| | 160 ± 3 | 4(+), SF = 0.470 | 134 | | 3.6% [4′(+)] | |
| | | 4′(−), SF = 0.406 | 91 | | | |
| | | 6(+), SF = 0.323 | 59 | | | |
| | | ***4′(+), SF = 0.279*** | 157 | 5th | | |
| G10 | 45 ± 2 | 4(−), SF = 0.468 | 41 | 1st | 6.2% [4(−)] | 5.3% |
| G11 | 33 ± 4 | 4′(+), SF = 0.424 | 31 | 1st | 5.2% [4′(+)] | 5.2% |
| | 150 ± 2 | 4′(−), SF = 0.406 | 147 | 2nd | 5.4% [4′(−)] | |
| G12[a] | 127 ± 1 | 6(+), SF = 0.477 | 61 | | 6.1% [6(−)] | 5.6% |
| | 37 ± 3 | ***6(−), SF = 0.476*** | 129 | 2nd | 4.1% [6′(+)] | |
| | | ***6′(+), SF = 0.315*** | 38 | 3rd | | |
| G13 | 34 ± 2 | 4(−), SF = 0.472 | 39 | 1st | 6.0% [4(−)] | 5.2% |
| | 133 ± 2 | 4(+), SF = 0.464 | 134 | 2nd | 5.9% [4(+)] | |
| G14 | 32 ± 3 | 3′(+), SF = 0.446 | 33 | 1st | 5.7% [3′(+)] | 6.8% |
| | 147 ± 4 | 3′(−), SF = 0.444 | 147 | 2nd | 5.7% [3′(−)] | |
| G15 | 33 ± 1 | 4(−), SF = 0.463 | 34 | 1st | 5.9% [4(−)] | 6.8% |
| G16[a] | 27 ± 1 | 3(−), SF = 0.447 | 38 | | | 3.8% |
| | 148 ± 3 | ***3(+), SF = 0.439*** | 144 | 2nd | 5.7% [3(+)] | |
| | | ***3′(−), SF = 0.369*** | 30 | 3rd | 4.8% [3′(−)] | |

[a] Non Schmid behaviour, ***bold/italic*** activated non-Schmid variants.

variant with the most negative SF should form during compression [60]. It can be thus concluded with confidence that some of the traces observed in grain G3 may are due to the activation of the HPV 4′(+). There are two reasons for that: (i) the theoretical trace inclination of HPV 4′(+) agrees well with the observed one (by HR-DIC) and more importantly (ii) its theoretical transformation strain agrees very well with that determined by HR-DIC, see Table 2. If the specific trace would be ascribed to e.g. slip only, criterion (ii) would not be fulfilled. Since in the majority of the grains, a strain recovery could be detected by HR-DIC, some traces can be safely attributed to the stress-induced formation of martensite. Additionally, Fig. 1f evidences that some plates completely vanish after unloading (shown with red arrows) which can only be ascribed to the presence of reversible martensite. Moreover, Mao et al. identified similar plates appearing in a superelastic NiTi alloy with large grains as martensite using EBSD [7]. As shown in Table 2, the locally recovered strains determined by HR-DIC are in good agreement with the theoretical transformation strains calculated for the formation of *HPVs* in single crystals. The transformation strain including detwinning of the initially twinned HPV under tension (the so-called transformation into lattice correspondent variants - LCVs), is about 10% for the crystallographic orientations of the investigated grains, which is higher than the measured recoverable strain. Therefore, the measured transformation strain agrees better with the predicted transformation strain originating from the formation of HPVs rather than LCVs. It should be noted that in the present study the grain size of 35 μm is large compared to the thickness of the sample (80 μm) and therefore constraints normally occurring in a polycrystal might be relaxed to some extent [50]. Hence, it is not surprising that the behaviour of each individual grain approaches the behaviour of a single crystal. In some grains (e.g. G8 and G16), the measured recoverable strain is lower than the theoretical transformation strain possibly due to partial reversibility of the stress-induced martensite.

In grains G1, G2, G3, G4, G5, G10 and G15, only the variant with the highest SF is found to be activated. In contrast, other grains (G7, G9, G11, G12, G13, G14, G16) exhibit two or more variants and in most cases include the highest-Schmid-factor HPVs. The activation of multiple HPVs in the same grain is in contrast with previous analytical studies [5,61] where the existence of only one martensite variant (with the highest SF) was considered. This led to an overestimation of the calculated transformation strain, since variants with highest SF exhibit the highest transformation strain, as discussed in Section 2.3. In summary, the recoverable strain is due to the reversible martensitic transformation. Despite grain interactions that cause multiaxial stress states at the intragranular lengthscale, the two other principal stress components are negligible compared to the applied stress component [49]. Therefore, the activation of the HPVs can be well predicted by application of the Schmid law assuming uniaxial tension, which is in good agreement with [6,7].

*4.1.2. Non Schmid behaviour and variant transfer across grain boundaries*

Grains G6, G9, G12 and G16 exhibit a deviation from the Schmid law as the activated variants do not have the highest Schmid factors (see Table 2). As illustrated in Fig. 2, the non-Schmid variants are a result of shear transmission across the grain boundaries. For example the HPV 4′(+) in G8 is transmitted across the grain boundary to G9 where it has the 5th highest SF, as shown in Tables 2 and 3. The formation of these variants can be rationalized with a geometrical compatibility factor, which predicts the transfer of slip between adjacent grains

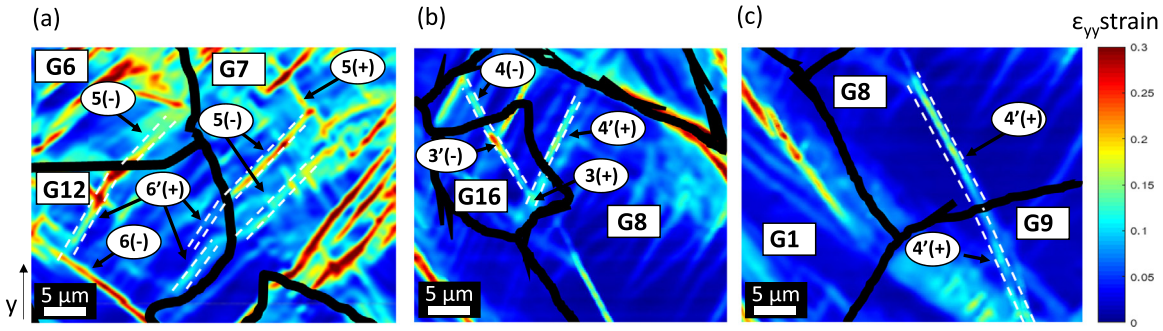


**Fig. 2.** Detailed local strain maps of (a) grains G6, G12, G7, (b) G16, G8 and (c) G8, G9 which exhibit non-Schmid behaviour. The transmission of traces of the habit plane variants is indicated by white dashed lines. The loading direction corresponds to the y-axis.

meanwhile maintaining coherency at the grain boundaries during homogeneous deformation of polycrystalline materials [62]. This approach has until now only been used to explain the transfer of twinning across grain boundaries in Mg alloys [63,64] or Ti alloys [65]. This factor, designated as $m'$, can be calculated from the knowledge of two angles: the angle, $\theta$, between the shear directions in grains *I* and *II*, and the angle, $\psi$, between the normal to the habit planes.

$$m\prime = cos\theta\ cos\psi \tag{5}$$

Table 3 lists the active variants of the neighboring grains, and the compatibility factor between the activated habit plane variants for the grains that show variants deviating from the Schmid law. For comparison, the compatibility factor between the highest SF variants and the active variants of the neighboring grains are given. It is observed that in two cases (grains G6 and G9) the variant transmitted through the boundary from the neighboring grain results in perfect compatibility, i.e., $m'$ is equal to 1. The activated "non Schmid" variant and the variant of the neighboring grain in G12 and G16 exhibit higher compatibility than the non-activated variants with the highest SF. In all cases however the SF values of the activated variants is relatively high (3rd or 5th highest out of the 24), as the resolved shear stress on the habit plane needs to be high enough.

The transmitted variants in G8-G16 are examples of variants with relatively low geometrical compatibility. The HPV pair 4′(+) and 3(+) in grains G8-G16 exhibits lower geometrical compatibility ($m' = 0.16$) than the HPV pair with the highest SF, i.e. 4′(+) and 3(−) ($m' = 0.4$). As mentioned already before, the behaviour of the grains agrees with the Schmid law assuming a pure uniaxial stress state in the grains, however, the small deviations on this rule can be explained by local stress concentrations or appearance of multiaxial stress state in the grain level.

### 4.2. Non-recoverable strain mechanisms

#### 4.2.1. Slip in austenite

The significant non-recoverable strain after unloading indicates the loss of superelasticity which is detrimental for the cycling stability of this material. Slip is one of the possible deformation mechanisms contributing to the non-recoverable strain after complete unloading. Table 4 lists for each austenite grain the observed non-recovered trace inclinations (shown in Fig. 1f) with respect to the loading direction and the expected trace inclinations for the {110}⟨100⟩ B2 slip system with the highest SF [66].

In Fig. 1f, grain G1 exhibits residual strain traces inclined 151 ± 2° with respect to the loading direction. The slip system with the highest SF (SF ≈ 0.40) would give a trace of 148° with respect to the loading direction. The second highest SF slip system (SF ≈ 0.38) has a trace of 123° with respect to the loading direction. Therefore, the non-recoverable traces observed in G1 with an inclination of 151 ± 2° can partially correspond to dislocation slip of the system with the highest SF.

In grain G5, the traces are hardly recovered (see Fig. 1d–f) and the trace inclination agrees relatively well with $(1\bar{1}0)[00\bar{1}]$ dislocation slip (see Table 4). Grain G5 has a significantly different crystallographic orientation compared to the rest of the grains. Its orientation, along the loading direction is close to ⟨001⟩, which is not favourable for the formation of stress induced martensite [60], thus slip seems to be the dominant mechanism despite that some recovered strain can also be attributed to the activation of one HPV variant (with the highest SF).

In grains G1, G2, G3, G4, G5, G8 and G13 the observed trace inclinations can be correlated with those belonging to the potential slip systems with one of the highest SFs (ranked first to third) with a tolerance of ±5°, but no correlation can be found for the traces seen in grains G6, G7, G9, G10, G11, G12; the irreversible strain in these grains can be due to other mechanisms that are discussed in the following sections. In summary, deformation by {110}⟨100⟩ B2 slip contributes to the irreversible strain shown in Fig. 1f.

#### 4.2.2. Deformation twinning

Looking closer to the strain traces in the HR-DIC maps, Fig. 3a and b show an example of the evolution of the trace morphology in G1 upon straining between 8% and 10% average strain. The straight bands at 8% average strain, develop to a "zig-zig" structure when the strain in the FOV increases to 10%, as shown in Fig. 3a. Similar "zig-zag" structures were also observed in several other grains such as in G2, G7, G9. The appearance of "zig-zag" structures and the significant increase of the strain, within the initially low strain trace due to martensite formation, suggests that an additional deformation mechanism succeeds the activation of martensite. After unloading

**Table 3**
List of grains exhibiting non-Schmid behaviour and geometric compatibility factors, $m'$, of the habit plane variants which are transmitted across grain boundaries, see Fig. 4.

| Grains showing deviation from the Schmid law | Activated variant [rank in SF value] | Transmitted variant [from neighboring grain(s)] | $m'$ of the activated variant and the neighboring variant | $m'$ of highest SF variant and the neighboring variant [variant] |
|---|---|---|---|---|
| G6 | 5(−) [2] | 5(−) [G7] | 1.00 | 0.87 [5(+)] |
| G9 | 4′(+) [5] | 4′(+) [G8] | 1.00 | −0.25 [4(+)] |
| G12 | 6′(+) [3] | 5(−) [G6/G7] | 0.40 | 0.16 [6(+)] |
| G16 | 3′(−) [3] | 4(−) [G8] | 0.16 | −0.16 [3(−)] |
| G16 | 3(+) [2] | 4′(+) [G8] | 0.16 | 0.4 [3(−)] |

**Table 4**
List of the grains and the observed and expected trace inclinations for the slip system {110}⟨100⟩ with the highest SF. The error represents the standard deviation of the inclination measured over several traces in each grain.

| Grain | Angle of trace with respect to loading direction from HR-DIC (degrees) | Highest SF slip system, SF value | Theoretical trace angle of highest SF (degrees) | Possible activated variant rank of SF |
|---|---|---|---|---|
| G1 | 151 ± 2 | (0−11)[100], SF = 0.399 | 148 | 1st |
| G2 | 143 ± 2 | (011)[−100], SF = 0.377 | 135 | 2nd |
| | | (1−10)[00−1], SF = 0.374 | 144 | |
| G3 | 153 ± 3 | (0–11)[100], SF = 0.336 | 154 | 1st |
| G4 | 37 ± 1 | (0–11)[−100], SF = 0.399 | 54 | 2nd |
| | | (110)[00–1], SF = 0.388 | 39 | |
| G5 | 155 ± 2 | (1–10)[00–1], SF = 0.193 | 164 | 1st |
| G6 | 50 ± 1 | (011)[−100], SF = 0.348 | 101 | No correlation |
| G7 | 141 ± 3 | (0–11)[100], SF = 0.334 | 156 | 3rd |
| | 46 ± 3 | (101)[0−10], SF = 0.327 | 98 | No correlation for the second trace |
| | | (−101)[010], SF = 0.298 | 141 | |
| G8 | 29 ± 4 | (0–11)[100], SF = 0.354 | 27 | 1st |
| G9 | 42 ± 1 | (011)[100], SF = 0.437 | 36 | 3rd |
| | 160 ± 3 | (110)[001], SF = 0.416 | 66 | No correlation for the second trace |
| | | (0–11)[100], SF = 0.248 | 156 | |
| G10 | 45 ± 2 | (011)[100], SF = 0.439 | 34 | No correlation |
| G11 | 33 ± 4 | (0–11)[100], SF = 0.345 | 146 | 1st |
| | 150 ± 2 | | | No correlation for the second trace |
| G12 | 127 ± 1 | (0–11)[100], SF = 0.372 | 23 | No correlation for either |
| | 37 ± 3 | | | |
| G13 | 34 ± 2 | (011)[100], SF = 0.417 | 34 | 1st |
| | 133 ± 2 | ….. | | |
| | | (0–11)[100], SF = 0.271 | 133 | 4th |
| G14 | 32 ± 3 | (0–11)[−100], SF = 0.382 | 137 | |
| | 147 ± 4 | …. | | |
| | | (1–10)[00–1], SF = 0.381 | 35 | 2nd |
| | | (1–10)[00–1], SF = 0.324 | 143 | 3rd |
| G15 | 33 ± 1 | (011)[100], SF = 0.408 | 39 | |
| | | ….. | | |
| | | (1–10)[001], SF = 0.290 | 29 | 3rd |
| G16 | 27 ± 1 | (011)[−100] SF = 0.376 | 124 | 2nd |
| | 148 ± 3 | (1–10)[00–1], SF = 0.369 | 143 | |
| | | … | …… | 4th |
| | | (0–11)[−100], SF = 0.307 | 23 | |

in G1, two regions within the "zig-zag" structure are indexed as austenitic phase with high confidence using EBSD. In addition to the matrix, two distinctly new austenite orientations appear, i.e. three austenite orientations exist in the grain. These regions within the "zig-zag" morphology have crystallographic orientations different from the initial parent grain, as shown in Fig. 3c, implying that a twinning mechanism occurs in austenite upon unloading. The noise seen as spots with different colours in Fig. 3c can be attributed to unindexed patterns. Due to overlapping interfaces of the two different austenite orientations, local high deformation at the interface of these bands and/or possible presence of small fractions of martensite, the indexing of the Kikuchi patterns is impossible.

The formation of twinned austenite, hereafter denoted as $B2^T$, via the sequence B2-B19'-$B2^T$, has been a topic of intensive research [13–16,67–69]. Similar microstructure reported in the literature is a result of either {112} austenite twins inherited from {113} martensite twins [69] or {114} austenite twins [13–16,70] inherited from $\{20\bar{1}\}$ martensite twins [70,71]. Ezaz et al. [68] showed the $\{20\bar{1}\}$ martensite twinning induced at early stages of plastic deformation of martensite, while {113} martensite twinning occurs at later stages of deformation or severe plastic deformation [69]. A recent series of comprehensive TEM studies supports that {114} austenite twinning appears after deformation beyond the yield point of martensite [13–16]. Another investigation claims that the appearance of {112} austenite twin is a misinterpretation of {114} twinning [72] while Goo et al. evoke the possibility of formation of disordered {112} twinning in B2, the so-called {112} pseudo twins [73].

Assuming {112} $B2^T$, the theoretical angle between two {112} planes bounding the "zig-zag", i.e. $(\bar{1}\bar{1}2)$ and $(\bar{1}\bar{2}1)$, should be ~33.6° and the projection of this angle on the sample surface should be ~17°. As for {114} $B2^T$, the theoretical angle between two {114} planes bounding the "zig-zag", i.e. $(\bar{1}4\bar{1})$ and $(14\bar{1})$, should be ~27.3° and the projection of this angle on sample surface should be ~23°, as shown in Fig. 3. The inclination between the traces observed on the EBSD map shown in Fig. 3c is in relatively good agreements (within ±3°) with both {112} $B2^T$ and {114} $B2^T$. The misorientation measured along the line drawn across the "zig-zag" bands in Fig. 3c correspond to 35° and 15° misorientation with respect to the parent grain, i.e. a misorientation of ~20° between the two regions forming the "zig-zag".

Fig. 4a shows a collection of bright field TEM images of the twin-related austenite microstructure (zig-zag features) within the previously transformed zone (HPV martensite). The red dashed lines indicate the interface of the austenite matrix and the twinned region, which is recognized as the HPV traces of either 4′(+) or 4′(−) (see Table 2). In the vicinity of the austenite/martensite boundary, significant diffraction contrast is due to dislocations formed during austenite slip as well as the martensitic transformation. Selected area diffraction patterns (SADP) taken outside and inside the "zig-zag" area (Fig. 4b and d–e) show three different austenitic orientations. Fig. 4b is a SADP of the parent grain in a [113]-type zone axis. While moving on the "zig-zag" bands without tilting, the SADP is no longer in a [113]-type zone axis, suggesting a misorientation with respect to the parent grain. Fig. 4d–e show the SADPs of the two observed new orientations (the two "zig-zig"), which are ~21° misoriented to each other, confirming the existence of twinned austenite.

The material in the present study was not severely deformed and the non-recoverable strain possibly occurs from stress concentrations due to variations in the sample cross-section area. It appears hence that the most possible deformation mechanism is {114} $B2^T$ inherited from $\{20\bar{1}\}$ martensite twins which only appear at early stages of martensite deformation. The exact type and the mechanism of the $B2^T$ formation

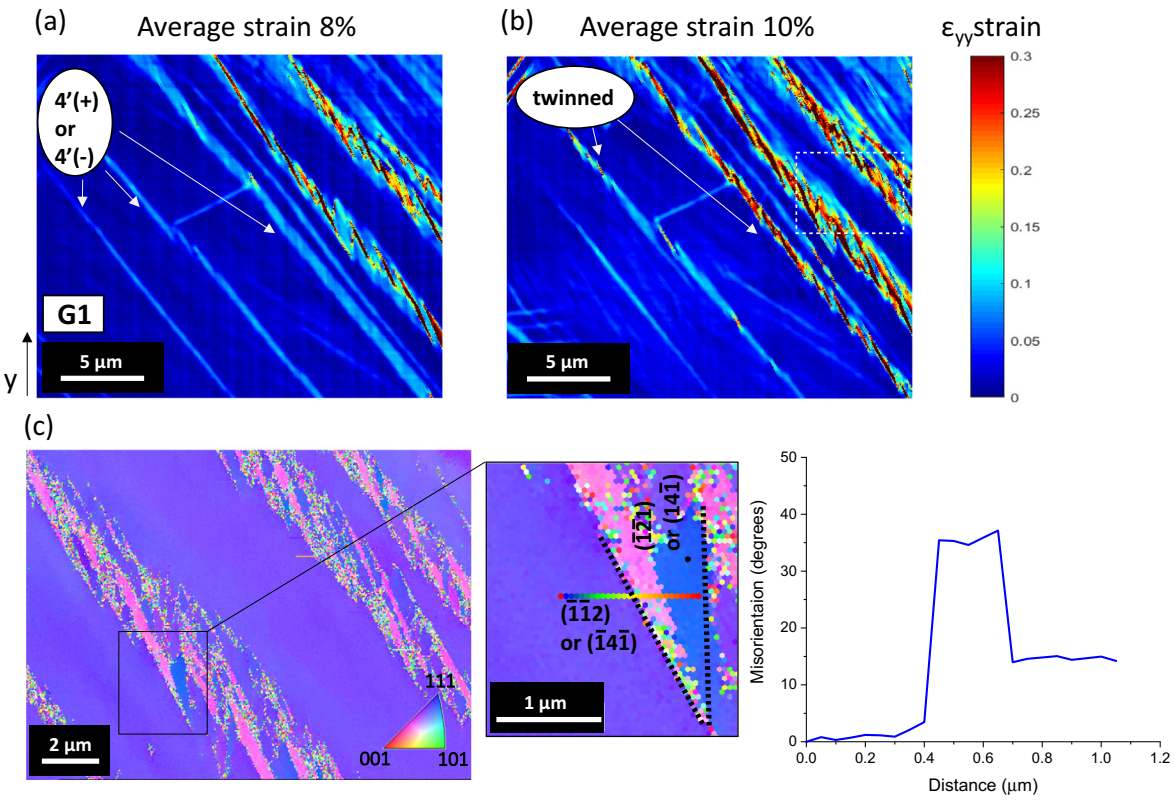


**Fig. 3.** Local strain maps obtained in grain G1 showing the evolution of the same bands at average strains of (a) 8% and (b) 10%. The dark red lines correspond to strain values more between 0.3 and 0.4 strain. The transformation of habit plane variants into "zig-zag" morphologies is seen by comparing (b) to (a). The white dashed line in (b) shows the approximate location of EBSD, after some gentle polishing. (c) EBSD map of the same bands in the same grain G1 (out of plane projection) after unloading showing that the "zig-zag" structure comprises of two austenite regions with different orientations ("pink"-⟨327⟩ and "blue"-⟨545⟩) with respect to the parent grain orientation ("purple"-⟨658⟩), a line scan (rainbow line) from the parent grain along the "zig-zag" structure shows 35° and 15° misorientation with respect to the orientation of the parent phase. The traces of the $(\bar{1}\bar{1}2)$or$(\bar{1}4\bar{1})$ and $(\bar{1}\bar{2}1)$or$(14\bar{1})$ planes are shown in (c) and align well with the "zig-zag" bands. The loading direction corresponds to the y-axis.

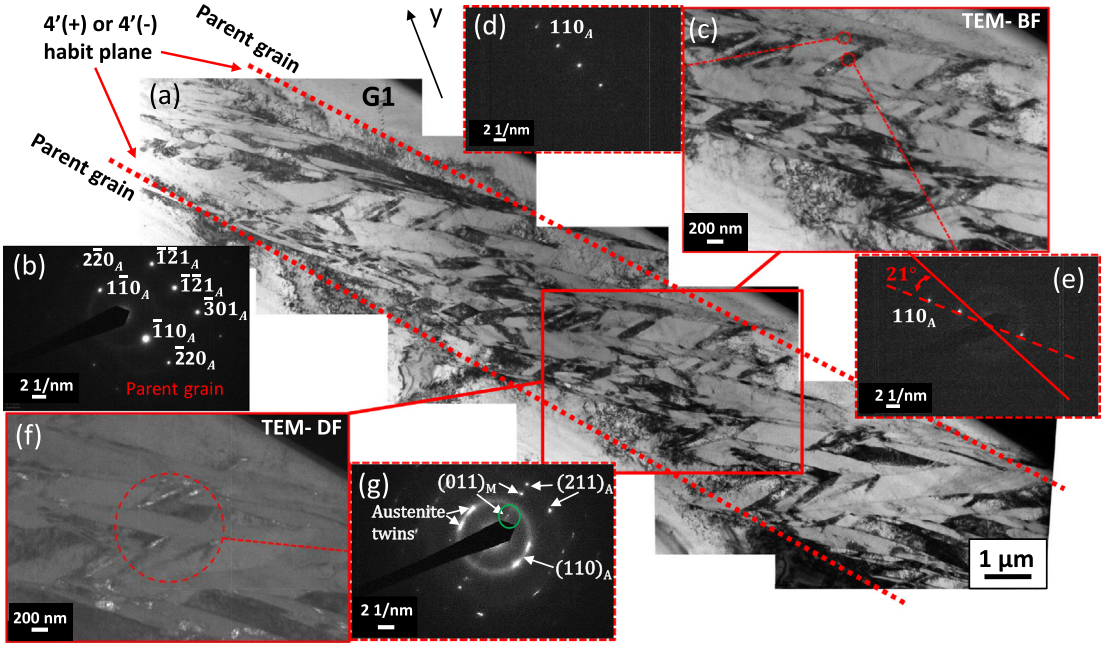


**Fig. 4.** (a) Montage of bright field TEM images showing the "zig-zag" structure which formed by deformation twinning inside a martensite variant (either 4′(+) or 4′(−)). (b) SADP of the parent grain, taken outside the "zig-zag" structure shown in (a). (c) Details of the area indicated with red square in (a) showing the "zig-zag" structure where two austenite orientations can be recognized. The corresponding diffraction patterns of these two austenite orientations are shown in (d) and (e), respectively, where a 20° misorientation can be measured. (f) Dark field image showing retained martensite as bright structures. The red circle in (f) indicates the position from where the SADP is taken. The spot used for the dark field imaging is highlighted with a green circle in (g). The loading direction corresponds to the y-axis.

requires further investigations which are currently not the target of this study.

Finally, TEM reveals the presence of small fractions of retained martensite as shown in Fig. 4f–g. Fig. 4f is a dark-field TEM image using the spot indexed as (011) martensite in Fig. 4g. Martensite appears to be locked in the microstructure at the intercepts of the "zig-zag" bands in good agreement with [13,16], however it is interestingly low in fraction. The small fraction of residual martensite is below the EBSD detection limit and therefore the "zig-zag" bands where indexed as fully austenitic. Residual martensite is another mechanism for accumulating residual strain.

In summary, part of the non-recoverable strain is due to residual martensite and due to the occurrence of austenite twinning upon reverse phase transformation, which is in good agreement with [13]. The fact that the "zig-zag" traces appear in bands already correlated to HPVs suggests that the austenite twinning is inherited from twinning in martensite, i.e. following the deformation sequence: B2-B19′-B2$^{T}$.

## 5. Conclusions

HRDIC in combination with EBSD is capable of capturing the recoverable and non-recoverable strain. In combination with TEM, the operation of multiple deformation mechanisms in a superelastic coarse-grained NiTi is revealed. Analysis based on the recoverable strain and trace inclination shows the activation of habit plane variants of martensite upon loading which revert to austenite after unloading. In more than half of the grains, two habit plane variants are observed. In the majority of the observed grains, the activated habit plane variants agree with the Schmid law i.e., the habit plane variant with the highest SF is activated, assuming that the macroscopic stress state occurs also within the grains. The observed "non-Schmid" habit plane variants are rationalized based on a transmission criterion across the grain boundary. The variant transmission occurs when the best compromise between the following two conditions is achieved: (1) the angle between the habit planes and the shear directions of the two variants activated on each side of the grain boundary have to be small (geometrical compatibility) and (2) the SF of the activated variants has to be high. The observed transformation strains correlate well with the theoretical estimates in single crystals. Besides the recoverable strain by martensitic transformation, non-recoverable strain is accommodated by dislocation slip in the austenite and austenite twinning following the sequence: B2-B19′-B2$^{T}$. Finally, small amounts of retained martensite are detected, contributing to the non-recoverable strain. The coexistence of stress-induced martensite, slip and twinning in martensite/austenite results in deformation bands with high axial strain.

## CRediT authorship contribution statement

**E. Polatidis:** Investigation, Data curation, Formal analysis, Writing - original draft. **M. Smid:** Investigation, Data curation, Formal analysis, Writing - review & editing. **I. Kubena:** Investigation, Data curation, Formal analysis, Writing - review & editing. **W.-N. Hsu:** Investigation, Data curation, Formal analysis, Writing - review & editing. **G. Laplanche:** Resources, Writing - review & editing. **H. Van Swygenhoven:** Supervision, Funding acquisition, Writing - review & editing.

## Declaration of competing interest

The authors declare that they have no known competing financial interests or personal relationships that could have appeared to influence the work reported in this paper.

## Acknowledgement

EP, MS, IK, W-NH and HVS thank the European Research Council for the ERC-advanced Grant MULTIAX (339245). IK acknowledges the Ministry of Education, Youth and Sports of the Czech Republic for the project m-IPMinfra (CZ.02.1.01/0.0/0.0/16_013/0001823). The infrastructure of IPMinfra were used for the TEM investigations. GL acknowledges funding from the Alexander von Humboldt Foundation. The authors acknowledge Dr. Rolf Brönnimann (EMPA, Dübendorf) for the assistance I n the sample preparation with the picosecond laser.

The raw/processed data required to reproduce these findings cannot be shared at this time as the data also forms part of an ongoing study.

## Appendix A. Supplementary data

Supplementary data to this article can be found online at https://doi.org/10.1016/j.matdes.2020.108622.

## References

[1] T. Duerig, A. Pelton, D. Stöckel, An overview of nitinol medical applications, Mater. Sci. Eng. A 273–275 (1999) 149–160, https://doi.org/10.1016/S0921-5093(99)00294-4.
[2] Y. Furuya, H. Shimada, Shape memory actuators for robotic applications, Mater. Des. 12 (1991) 21–28, https://doi.org/10.1016/0261-3069(91)90088-L.
[3] K. Gall, H. Sehitoglu, The role of texture in tension–compression asymmetry in polycrystalline NiTi, Int. J. Plast. 15 (1999) 69–92, https://doi.org/10.1016/S0749-6419(98)00060-6.
[4] H. Sehitoglu, I. Karaman, R. Anderson, X. Zhang, K. Gall, H.J. Maier, Y. Chumlyakov, Compressive response of NiTi single crystals, Acta Mater. 48 (2000) 3311–3326, https://doi.org/10.1016/S1359-6454(00)00153-1.
[5] Y. Liu, The superelastic anisotropy in a NiTi shape memory alloy thin sheet, Acta Mater. 95 (2015) 411–427, https://doi.org/10.1016/j.actamat.2015.03.022.
[6] S.C. Mao, X.D. Han, Y.B. Tian, J.F. Luo, Z. Zhang, Y. Ji, M.H. Wu, In situ EBSD investigations of the asymmetric stress-induced martensitic transformation in TiNi shape memory alloys under bending, Mater. Sci. Eng. A 498 (2008) 278–282, https://doi.org/10.1016/j.msea.2008.07.072.
[7] S.C. Mao, J.F. Luo, Z. Zhang, M.H. Wu, Y. Liu, X.D. Han, EBSD studies of the stress-induced B2–B19′ martensitic transformation in NiTi tubes under uniaxial tension and compression, Acta Mater. 58 (2010) 3357–3366, https://doi.org/10.1016/j.actamat.2010.02.009.
[8] G. Laplanche, J. Pfetzing-Micklich, G. Eggeler, Sudden stress-induced transformation events during nanoindentation of NiTi shape memory alloys, Acta Mater. 78 (2014) 144–160, https://doi.org/10.1016/j.actamat.2014.05.061.
[9] D.M. Norfleet, P.M. Sarosi, S. Manchiraju, M.F.X. Wagner, M.D. Uchic, P.M. Anderson, M.J. Mills, Transformation-induced plasticity during pseudoelastic deformation in Ni–Ti microcrystals, Acta Mater. 57 (2009) 3549–3561, https://doi.org/10.1016/j.actamat.2009.04.009.
[10] T. Simon, A. Kröger, C. Somsen, A. Dlouhy, G. Eggeler, On the multiplication of dislocations during martensitic transformations in NiTi shape memory alloys, Acta Mater. 58 (2010) 1850–1860, https://doi.org/10.1016/j.actamat.2009.11.028.
[11] M.L. Bowers, X. Chen, M. De Graef, P.M. Anderson, M.J. Mills, Characterization and modeling of defects generated in pseudoelastically deformed NiTi microcrystals, Scr. Mater. 78–79 (2014) 69–72, https://doi.org/10.1016/j.scriptamat.2014.02.001.
[12] R. Delville, B. Malard, J. Pilch, P. Sittner, D. Schryvers, Transmission electron microscopy investigation of dislocation slip during superelastic cycling of Ni–Ti wires, Int. J. Plast. 27 (2011) 282–297, https://doi.org/10.1016/j.ijplas.2010.05.005.
[13] Y. Chen, O. Molnárová, O. Tyc, L. Kadeřávek, L. Heller, P. Šittner, Recoverability of large strains and deformation twinning in martensite during tensile deformation of NiTi shape memory alloy polycrystals, Acta Mater. 180 (2019) 243–259, https://doi.org/10.1016/j.actamat.2019.09.012.
[14] P. Šittner, L. Heller, P. Sedlák, Y. Chen, O. Tyc, O. Molnárová, L. Kadeřávek, H. Seiner, B2 ⇒ B19′ ⇒ B2$^{T}$ martensitic transformation as a mechanism of plastic deformation of NiTi, Shap. Mem. Superelasticity 2019, pp. 1–14, https://doi.org/10.1007/s40830-019-00250-5.
[15] Y. Chen, O. Tyc, L. Kadeřávek, O. Molnárová, L. Heller, P. Šittner, Temperature and microstructure dependence of localized tensile deformation of superelastic NiTi wires, Mater. Des. 174 (2019), 107797. https://doi.org/10.1016/j.matdes.2019.107797.
[16] P. Šittner, O. Molnárová, L. Kadeřávek, O. Tyc, L. Heller, Deformation twinning in martensite affecting functional behavior of NiTi shape memory alloys, Materialia 9 (2020), 100506. https://doi.org/10.1016/j.mtla.2019.100506.
[17] F. Di Gioacchino, J.Q. da Fonseca, Plastic strain mapping with sub-micron resolution using digital image correlation, Exp. Mech. 53 (2013) 743–754.
[18] C.C. Tasan, J.P.M. Hoefnagels, M. Diehl, D. Yan, F. Roters, D. Raabe, Strain localization and damage in dual phase steels investigated by coupled in-situ deformation experiments and crystal plasticity simulations, Int. J. Plast. 63 (2014) 198–210, https://doi.org/10.1016/j.ijplas.2014.06.004.
[19] F. Di Gioacchino, J. Quinta da Fonseca, An experimental study of the polycrystalline plasticity of austenitic stainless steel, Int. J. Plast. 74 (2015) 92–109, https://doi.org/10.1016/j.ijplas.2015.05.012.
[20] Y.B. Das, A.N. Forsey, T.H. Simm, K.M. Perkins, M.E. Fitzpatrick, S. Gungor, R.J. Moat, In situ observation of strain and phase transformation in plastically deformed 301 austenitic stainless steel, Mater. Des. 112 (2016) 107–116, https://doi.org/10.1016/j.matdes.2016.09.057.

[21] E. Polatidis, W.-N. Hsu, M. Šmíd, H. Van Swygenhoven, A high resolution digital image correlation study under multiaxial loading, Exp. Mech. 59 (2019) 309–317, https://doi.org/10.1007/s11340-018-00443-6.

[22] D. Yan, C.C. Tasan, D. Raabe, High resolution in situ mapping of microstrain and microstructure evolution reveals damage resistance criteria in dual phase steels, Acta Mater. 96 (2015) 399–409, https://doi.org/10.1016/j.actamat.2015.05.038.

[23] D. Lunt, T. Busolo, X. Xu, J. Quinta da Fonseca, M. Preuss, Effect of nanoscale α2 precipitation on strain localisation in a two-phase Ti-alloy, Acta Mater. 129 (January 5 2017) 72–82, https://doi.org/10.1016/j.actamat.2017.02.068.

[24] A. Orozco-Caballero, D. Lunt, J.D. Robson, J. Quinta da Fonseca, How magnesium accommodates local deformation incompatibility: a high-resolution digital image correlation study, Acta Mater. 133 (2017) 367–379, https://doi.org/10.1016/j.actamat.2017.05.040.

[25] P. Platt, D. Lunt, E. Polatidis, M.R. Wenman, M. Preuss, In-situ digital image correlation for fracture analysis of oxides formed on zirconium alloys, Corros. Sci. 111 (2016) 344–351, https://doi.org/10.1016/j.corsci.2016.05.026.

[26] X. Xie, Q. Kan, G. Kang, J. Li, B. Qiu, C. Yu, Observation on the transformation domains of super-elastic NiTi shape memory alloy and their evolutions during cyclic loading, Smart Mater. Struct. 25 (2016), 045003. https://doi.org/10.1088/0964-1726/25/4/045003.

[27] X. Xie, Q. Kan, G. Kang, F. Lu, K. Chen, Observation on rate-dependent cyclic transformation domain of super-elastic NiTi shape memory alloy, Mater. Sci. Eng. A 671 (2016) 32–47, https://doi.org/10.1016/j.msea.2016.06.045.

[28] X. Bian, A.A. Saleh, E.V. Pereloma, C.H.J. Davies, A.A. Gazder, A digital image correlation study of a NiTi alloy subjected to monotonic uniaxial and cyclic loading-unloading in tension, Mater. Sci. Eng. A 726 (2018) 102–112, https://doi.org/10.1016/j.msea.2018.04.081.

[29] J. Lackmann, T. Niendorf, M. Maxisch, G. Grundmeier, H.J. Maier, High-resolution in-situ characterization of the surface evolution of a polycrystalline NiTi SMA-alloy under pseudoelastic deformation, Mater. Charact. 62 (2011) 298–303, https://doi.org/10.1016/j.matchar.2010.12.008.

[30] M. Kimiecik, J. Wayne Jones, S. Daly, Grain orientation dependence of phase transformation in the shape memory alloy nickel–titanium, Acta Mater. 94 (2015) 214–223, https://doi.org/10.1016/j.actamat.2015.04.026.

[31] W.-N. Hsu, E. Polatidis, M. Šmíd, N. Casati, S. Van Petegem, H. Van Swygenhoven, Load path change on superelastic NiTi alloys: in situ synchrotron XRD and SEM DIC, Acta Mater. 144 (2018) 874–883, https://doi.org/10.1016/j.actamat.2017.11.035.

[32] L. Heller, P. Šittner, P. Sedlák, H. Seiner, O. Tyc, L. Kadeřávek, P. Sedmák, M. Vronka, Beyond the strain recoverability of martensitic transformation in NiTi, Int. J. Plast. 116 (2019) 232–264, https://doi.org/10.1016/j.ijplas.2019.01.007.

[33] H. Sehitoglu, Y. Wu, S. Alkan, E. Ertekin, Plastic deformation of B2-NiTi – is it slip or twinning? Philos. Mag. Lett. 97 (2017) 217–228, https://doi.org/10.1080/09500839.2017.1316019.

[34] O. Shchyglo, U. Salman, A. Finel, Martensitic phase transformations in Ni–Ti-based shape memory alloys: the Landau theory, Acta Mater. 60 (2012) 6784–6792, https://doi.org/10.1016/j.actamat.2012.08.056.

[35] V.I. Levitas, A.M. Roy, D.L. Preston, Multiple twinning and variant-variant transformations in martensite: phase-field approach, Phys. Rev. B 88 (2013), 054113. https://doi.org/10.1103/PhysRevB.88.054113.

[36] Y. Zhong, T. Zhu, Phase-field modeling of martensitic microstructure in NiTi shape memory alloys, Acta Mater. 75 (2014) 337–347, https://doi.org/10.1016/j.actamat.2014.04.013.

[37] V.I. Levitas, A.M. Roy, Multiphase phase field theory for temperature- and stress-induced phase transformations, Phys. Rev. B 91 (2015), 174109. https://doi.org/10.1103/PhysRevB.91.174109.

[38] G. Laplanche, A. Kazuch, G. Eggeler, Processing of NiTi shape memory sheets – microstructural heterogeneity and evolution of texture, J. Alloys Compd. 651 (2015) 333–339, https://doi.org/10.1016/j.jallcom.2015.08.127.

[39] S.M. Guo, M.A. Sutton, N. Li, X.D. Li, L.W. Wang, S. Rajan, Measurement of local thermal deformations in heterogeneous microstructures via SEM imaging with digital image correlation, Exp. Mech. 57 (2017) 41–56, https://doi.org/10.1007/s11340-016-0206-6.

[40] J.P.M. Hoefnagels, M.P.F.H.L. van Maris, T. Vermeij, One-step deposition of nano-to-micron-scalable, high-quality digital image correlation patterns for high-strain in-situ multi-microscopy testing, Strain 55 (2019), e12330. https://doi.org/10.1111/str.12330.

[41] C.B. Montgomery, B. Koohbor, N.R. Sottos, A robust patterning technique for electron microscopy-based digital image correlation at sub-micron resolutions, Exp. Mech. 59 (2019) 1063–1073, https://doi.org/10.1007/s11340-019-00487-2.

[42] S. Van Petegem, A. Guitton, M. Dupraz, A. Bollhalder, K. Sofinowski, M.V. Upadhyay, H. Van Swygenhoven, A miniaturized biaxial deformation rig for in situ mechanical testing, Exp. Mech. 57 (2017) 569–580, https://doi.org/10.1007/s11340-016-0244-0.

[43] P. Sittner, Y. Liu, V. Novak, On the origin of Lüders-like deformation of NiTi shape memory alloys, J. Mech. Phys. Solids 53 (2005) 1719–1746, https://doi.org/10.1016/j.jmps.2005.03.005.

[44] E. Polatidis, N. Zotov, E. Bischoff, E.J. Mittemeijer, The effect of cyclic tensile loading on the stress-induced transformation mechanism in superelastic NiTi alloys: an in-situ X-ray diffraction study, Scr. Mater. 100 (2015) 59–62, https://doi.org/10.1016/j.scriptamat.2014.12.013.

[45] N. Zotov, M. Pfund, E. Polatidis, A.F. Mark, E.J. Mittemeijer, Change of transformation mechanism during pseudoelastic cycling of NiTi shape memory alloys, Mater. Sci. Eng. A 682 (2017) 178–191, https://doi.org/10.1016/j.msea.2016.11.052.

[46] G. Laplanche, T. Birk, S. Schneider, J. Frenzel, G. Eggeler, Effect of temperature and texture on the reorientation of martensite variants in NiTi shape memory alloys, Acta Mater. 127 (2017) 143–152, https://doi.org/10.1016/j.actamat.2017.01.023.

[47] Y. Xiao, P. Zeng, L. Lei, Y. Zhang, In situ observation on temperature dependence of martensitic transformation and plastic deformation in superelastic NiTi shape memory alloy, Mater. Des. 134 (2017) 111–120, https://doi.org/10.1016/j.matdes.2017.08.037.

[48] E. Polatidis, N. Zotov, E.J. Mittemeijer, Stress-induced phase transformations in thermally cycled superelastic NiTi alloys: in situ X-ray diffraction studies, Powder Diffract. 30 (2015) S76–S82, https://doi.org/10.1017/S0885715614001456.

[49] P. Sedmák, J. Pilch, L. Heller, J. Kopeček, J. Wright, P. Sedlák, M. Frost, P. Šittner, Grain-resolved analysis of localized deformation in nickel-titanium wire under tensile load, Science 353 (2016) 559–562, https://doi.org/10.1126/science.aad6700.

[50] Y. Sutou, T. Omori, R. Kainuma, K. Ishida, Grain size dependence of pseudoelasticity in polycrystalline Cu–Al–Mn-based shape memory sheets, Acta Mater. 61 (2013) 3842–3850, https://doi.org/10.1016/j.actamat.2013.03.022.

[51] J. Blaber, B. Adair, A. Antoniou, Ncorr: open-source 2D digital image correlation Matlab software, Exp. Mech. 55 (2015) 1105–1122, https://doi.org/10.1007/s11340-015-0009-1.

[52] MechMicroMan/DefDAP, Mechanics of microstructures at Manchester, 2019 . https://github.com/MechMicroMan/DefDAP , (accessed December 17, 2019).

[53] O. Matsumoto, S. Miyazaki, K. Otsuka, H. Tamura, Crystallography of martensitic transformation in Ti-Ni single crystals, Acta Metall.. 35 (8) 2137–2144. doi:https://doi.org/10.1016/0001-6160(87)90042-3.

[54] S. Miyazaki, K. Otsuka, C.M. Wayman, The shape memory mechanism associated with the martensitic transformation in Ti-Ni alloys—I. Self-accommodation, Acta Metall. 37 (1989) 1873–1884, https://doi.org/10.1016/0001-6160(89)90072-2.

[55] S.C. Mao, X.D. Han, Z. Zhang, The nano- and mesoscopic cooperative collective mechanisms of inhomogenous elastic-plastic transitions in polycrystalline TiNi shape memory alloys, J. Appl. Phys. 101 (2007), 103522. https://doi.org/10.1063/1.2722239.

[56] H. Sehitoglu, J. Jun, X. Zhang, I. Karaman, Y. Chumlyakov, H.J. Maier, K. Gall, Shape memory and pseudoelastic behavior of 51.5%Ni–Ti single crystals in solutionized and overaged state, Acta Mater. 49 (2001) 3609–3620, https://doi.org/10.1016/S1359-6454(01)00216-6.

[57] X. Zhang, H. Sehitoglu, Crystallography of the B2 → R → B19′ phase transformations in NiTi, Mater. Sci. Eng. A 374 (2004) 292–302, https://doi.org/10.1016/j.msea.2004.03.013.

[58] K. Otsuka, C.M. Wayman, K. Nakai, H. Sakamoto, K. Shimizu, Superelasticity effects and stress-induced martensitic transformations in Cu-Al-Ni alloys, Acta Metall. 24 (1976) 207–226, https://doi.org/10.1016/0001-6160(76)90071-7.

[59] W.-N. Hsu, E. Polatidis, M. Šmíd, S. Van Petegem, N. Casati, H. Van Swygenhoven, Deformation and degradation of superelastic NiTi under multiaxial loading, Acta Mater. 167 (2019) 149–158, https://doi.org/10.1016/j.actamat.2019.01.047.

[60] K. Gall, H. Sehitoglu, Y.I. Chumlyakov, I.V. Kireeva, Tension–compression asymmetry of the stress–strain response in aged single crystal and polycrystalline NiTi, Acta Mater. 47 (1999) 1203–1217, https://doi.org/10.1016/S1359-6454(98)00432-7.

[61] W.Q. Yuan, S. Yi, Pseudo-elastic strain estimation of textured TiNi shape memory alloys, Mater. Sci. Eng. A 271 (1999) 439–448, https://doi.org/10.1016/S0921-5093(99)00311-1.

[62] J. Luster, M.A. Morris, Compatibility of deformation in two-phase Ti-Al alloys: dependence on microstructure and orientation relationships, Metall. Mater. Trans. A 26 (1995) 1745–1756, https://doi.org/10.1007/bf02670762.

[63] C. Guo, R. Xin, C. Ding, B. Song, Q. Liu, Understanding of variant selection and twin patterns in compressed Mg alloy sheets via combined analysis of Schmid factor and strain compatibility factor, Mater. Sci. Eng. A 609 (2014) 92–101, https://doi.org/10.1016/j.msea.2014.04.103.

[64] H. Yu, Y. Xin, A. Chapuis, X. Huang, R. Xin, Q. Liu, The different effects of twin boundary and grain boundary on reducing tension-compression yield asymmetry of Mg alloys, Sci. Rep. 6 (2016), 29283. https://doi.org/10.1038/srep29283.

[65] F. Lin, M. Marteleur, P.J. Jacques, L. Delannay, Transmission of {332}⟨113⟩ twins across grain boundaries in a metastable β-titanium alloy, Int. J. Plast. 105 (2018) 195–210, https://doi.org/10.1016/j.ijplas.2018.02.012.

[66] T. Ezaz, J. Wang, H. Sehitoglu, H.J. Maier, Plastic deformation of NiTi shape memory alloys, Acta Mater. 61 (2013) 67–78, https://doi.org/10.1016/j.actamat.2012.09.023.

[67] A.N. Tyumentsev, N.S. Surikova, I.Yu. Litovchenko, Yu.P. Pinzhin, A.D. Korotaev, O.V. Lysenko, Mechanism of deformation and crystal lattice reorientation in strain localization bands and deformation twins of the B2 phase of titanium nickelide, Acta Mater. 52 (2004) 2067–2074, https://doi.org/10.1016/j.actamat.2004.01.001.

[68] T. Ezaz, H. Sehitoglu, W. Abuzaid, H.J. Maier, Higher order twin modes in martensitic NiTi—the (201¯) case, Mater. Sci. Eng. A 558 (2012) 422–430, https://doi.org/10.1016/j.msea.2012.08.022.

[69] I. Karaman, A.V. Kulkarni, Z.P. Luo, Transformation behaviour and unusual twinning in a NiTi shape memory alloy ausformed using equal channel angular extrusion, Philos. Mag. 85 (2005) 1729–1745, https://doi.org/10.1080/14786430412331331961.

[70] J.X. Zhang, M. Sato, A. Ishida, Deformation mechanism of martensite in Ti-rich Ti–Ni shape memory alloy thin films, Acta Mater. 54 (2006) 1185–1198, https://doi.org/10.1016/j.actamat.2005.10.046.

[71] S. Ii, K. Yamauchi, Y. Maruhashi, M. Nishida, Direct evidence of correlation between {201}B19′ and {114}B2 deformation twins in Ti–Ni shape memory alloy, Scr. Mater. 49 (2003) 723–727, https://doi.org/10.1016/S1359-6462(03)00356-7.

[72] M. Krishnan, B.C. Maji, Is the observation of {112} pseudotwins in the B2 phase of Ni-Ti-Fe shape-memory alloys a case of misidentification? Philos. Mag. Lett. 81 (2001) 243–249, https://doi.org/10.1080/09500830010029418.

[73] E. Goo, T. Duerig, K. Melton, R. Sinclair, Mechanical twinning in Ti50Ni47Fe3 and Ti49Ni51 alloys, Acta Metall. 33 (1985) 1725–1733, https://doi.org/10.1016/0001-6160(85)90167-1.